Spatial frequency-based angular behavior of a short-range flicker-free MIMO–OCC link

Shivani Rajendra Teli, Stanislav Zvanovec, Rafael Perez-Jimenez, Zabih Ghassemlooy

Spatial frequency-based angular behavior of a short-range flicker-free MIMO-OCC link

SHIVANI RAJENDRA TELI,[1, *] **STANISLAV ZVANOVEC,**[1] **RAFAEL PEREZ-JIMENEZ,**[2] **AND ZABIH GHASSEMLOOY**[3]

[1]*Department of Electromagnetic Field, Faculty of Electrical Engineering, Czech Technical University in Prague, Technicka, Prague 16627, Czech Republic*
[2]*IDeTIC, Universidad de Las Palmas de Gran Canaria, Las Palmas 35001, Spain*
[3]*Optical Communications Research Group, Faculty of Engineering and Environment, Northumbria University, Newcastle NE1 7RU, UK*
*Corresponding author: telishiv@fel.cvut.cz

In this paper, we provide a spatial frequency f_{sf} based solution to study the angular behavior of a flicker-free short-range indoor multiple-input multiple-output (MIMO) optical camera communication (OCC) link. We focus on the experimental investigation of OCC's performance for the transmitters (Txs) (i.e., light emitting diode (LED)- based arrays) located at the same and different distances from the receiver (Rx) with the off-axis rotation angle θ. We have used, two 8 × 8 distributed LED array and a commercial low-cost complementary metal-oxide-semiconductor (CMOS) Raspberry Pi camera with the rolling-shutter capturing mode as the Tx and Rx, respectively. The image and the respective communications link quality metrics are measured in terms of the peak signal-to-noise ratio (PSNR) and the rate of successfully received bits with respect to f_{sf} for different camera shutter speeds (SS). A CMOS image sensor noise characterization is carried in terms of the signal-to-noise ratio (SNR) and PSNR. The proposed study provides 100 % success rate in data reception at the optimum θ of 50° at lower captured values of f_{sf}, which is projected onto the image sensor in the form of pixels. Moreover, the effect of channel saturation over f_{sf} is studied with respect to θ and SS and we show that, for θ exceeding the optimum value along transmission range the f_{sf} area of the Txs reduces to less than ~50 % of the captured Tx units at θ of 0°, where no data can be fully recovered.

1. INTRODUCTION

The rapid advances made in development of a range of complementary metal-oxide-semiconductor (CMOS)-based camera (image sensors (IS)), which are used in mobile phones (front/rear camera), digital single-lens reflex cameras with higher capture speeds (ranging from 30 to 1000 fps) and surveillance cameras, have recently motivated research and development in camera-based visible light communications (VLC) also known as optical camera communications (OCC) in IEEE 802.15.7r1 Task Group [1, 2]. The CMOS cameras can capture images or record videos in global shutter (GS)- and rolling shutter (RS)-based capturing modes at different shutter speeds (SS) and resolutions.

In VLC links with light emitting diode (LED)-based transmitters (Txs), a wide range of dimming levels with no flickering can be adopted to ensure both illumination and data communications [3]. The IEEE 802.15.7 VLC standard outlines the maximum allowed flickering time period (MFTP) of 5 ms (i.e., 200 Hz) [4]. However, consumer-grade cameras have a limited capture rate of approximately 60 frames per second (fps). As a result, signals in OCC links can be captured at a very low sampling rate compared with the data transmission rate, thus resulting in the loss of unsampled data and lower probability of signal detection. Moreover, in OCC synchronization should be considered carefully by means of signaling, which reduces the data throughput [5]. Furthermore, a combination of LED-array Txs and OCC with photodetector (PD)-array can be used as massive multiple-input multiple-output (MIMO) to deliver parallel transmission and therefore higher data rates R_b in a range of applications including massive

internet of things (IoT) [6, 7]. Unlike the conventional PD-based Rx used in VLC, where the separation of mixed signals is not possible, the CMOS-based IS can capture lights coming from different directions and project them onto different sections of the IS (i.e., illuminating different PDs) [7]. Therefore, in these scenarios' spatial separation of incoming light signals and their intensities can be determined by measuring the pixel value per light source images on the received frame. The data from the pixelated images can then be recovered from the captured image frames using image processing algorithm implemented in MATLAB, OpenCV and Python [7]. In this approach, the CMOS IS can be used as the MIMO-OCC Rx without the need for extended hardware. For commercial use, a number of applications have been developed including OCC for the automotive industry by Intel® (USA) [8] and for online-to-offline marketing service by Panasonic (Japan) [9].

Although OCC does not support high-capacity transmission links, which is due to the speed limit of cameras, it can be employed in numerous low R_b and short range indoor and outdoor IoT applications including device-to-device communications, indoor positioning, localization, navigation, intelligent transportation system, financial transactions, motion-based device control, small identification information, communications through advertisements, etc. [3, 10, 11]. Note, in IoT-based smart environments, links with R_b of a few kbps are sufficient for information transmission and therefore there is no need for medium speed transmission capabilities. However, the major challenge in implementing systems with low R_b is the requirement for flicker-free transmission. Authors established flicker free communication links using grouped LED array concept in [12] using

RS-based capturing Rx with R_b of ~1 kbps. The RS acquisition mechanism that sequentially integrates light on rows of pixels is the major advantage of CMOS IS used as the Rx in OCC [13].

In OCC, the transmitted light signal will arrive at the Rx (i.e., IS) via both the line-of-sight (LOS) and non-LOS (NLOS) paths. However, the LOS becomes the dominant path when using Txs and Rxs with very narrow field of views. The RS-based MIMO-OCC transmission links are outlined below:

a. *LOS MIMO-OCC links:* Traditional indoor VLC or LOS OCC links with high R_b over a range of transmission spans have been adopted in many applications including (*i*) short-range RS-based indoor MIMO-OCC LOS (1-5 m) flicker-free links using multilevel intensity modulation (IM) with R_b of 10 kbps [14]; (*ii*) a beacon jointed packet reconstruction scheme with R_b of 5.76 kbps [15]; (*iii*) screen modulation techniques followed by the 2*M*-ary quadrature-amplitude modulation format [16]; (*iv*) a CMOS RS effect-based scheme using the grayscale value distribution and machine learning algorithm to enhance R_b [17]; and (*v*) the raptor code with linear time encoding and decoding with R_b of 1 kbps [18]. Note, in LOS-based systems it is possible some NLOS may be detected at the Rx, which will result in time delay spread.

b. *NLOS MIMO-OCC links:* In some scenarios such as device-to-device communications, it is possible that there might not be a LOS path between the Txs and the Rxs. Therefore, the communications will be via the NLOS paths, which offer mobility and flexibility but at the cost of lower R_b [19, 20]. NLOS-MIMO links based on space and time division multiple access technique with R_b of ~1 kbps and flicker-free transmission over a 10 m link span was reported in [19]. A 152 bits NLOS link (1.5 m) with a low level of error correction code using image processing techniques such as background compensation blooming mitigation, extinction-ratio enhancement and Bradley adaptive thresholding for RS demodulation was investigated in [21].

c. *Tx and Rx orientations:* Unlike previous studies, which focused on either a LOS or NLOS link, in MIMO-OCC links we need to considered both the Tx and Rx orientation angles. Some practical solutions considering different orientations and placements of the Tx and the Rx to support mobility scenarios in an indoor environment needs to be focused. In [6], the angular rotation θ from 0° to 70° along with parallel movement of a red, green and blue (RGB)-based LED array (16 × 16 LEDs) Tx and a 330-fps camera-based Rx operating in the GS capturing mode over a link span of 60 cm was reported. Note, in [6], the refresh rate for the LED array was set to 82 Hz, which is less than the MFTP standard rate of 200 Hz [4], thus providing flickering transmission and rotation support over a link span of 60 cm [6]. On the other hand, 60-LED-based array is used to provide both data transmission and frame synchronization. In [22], a practical orientation independent RS-based NOLS OCC link performing wide Rx's orientation for indoor applications with R_b of ~ 7 kbps over a transmission link span of 50 cm was presented. However, the Tx should be designed in such a way to ensure that there are sufficient reflections from many directions to ensure link availability. In [23], a CMOS RS pattern decoding scheme using the grayscale redistribution and differential grayscale packet selection was proposed and investigated to improve the decoding performance of the links under translational or rotational motions. The authors showed no significant signal degradation over a transmission range of up to 150 cm. Note, in applications with mobility, to ensure link availability, it is necessary to investigate various transmission scenarios considering different Txs angular orientations heights and distances from each other as well as from the Rx.

In this paper, we study multi-channel MIMO-OCC considering the angular rotation of the Txs located at the same distance but different heights and distances from each other. These transmission setups are defined considering the indoor dynamic, mobility and multicasting scenarios as in shopping malls, hospitals, offices, etc., where the number of Txs can be placed at different locations with different angles depending on the interior designs and the illumination requirements. The proposed scheme offers a valid solution irrespective of the availability of LOS and NLOS paths. It is based on the optimum angular orientation of multiple Tx units for practical indoor IoT-based scenarios such as mobility and multi-Tx/Rx (multiuser). The proposed scheme employs two MIMO-OCC Tx units with simplified design and a commercial low cost Raspberry Pi camera (RaspiCam) as the Rx. The lab-scale experiments are carried out for two different transmission setups, where the effect of optimum angular orientation θ of two Tx units located at different heights and distances from each other as well as the camera-based Rx is analyzed. For this reason, the spatial frequency f_{sf}, which represents the projection of a target, i.e., the Tx LED array over a captured image in terms of pixels, is used. The quality matrices of the captured image in terms of the peak signal-to-noise (PSNR) and the success rate of received bit sequences for a range of θ with respect to f_{sf}, L and SS are also analyzed.

The remainder of the paper is organized as follows: Section 2 describes the proposed MIMO-OCC system, Section 3 shows the measurement setup followed by Section 4 experiment results and analysis. Conclusions are drawn in Section 5.

2. PROPOSED MIMO-OCC SYSTEM

A. CMOS IS noise characterization within MIMO-OCC

The block diagram of the proposed MIMO-OCC system with multiple Txs (Tx_1–Tx_n) and IS Rx is shown in Fig. 1(a). At the Tx, the data is generated in the form of on-off keying non-return to zero (OOK-NRZ) format $s(t)$ and is used for IM of the LED via the LED driver. At the Rx, using an optical lens the IS captures multiple light Txs as different point sources on different sections of the IS. It is therefore straightforward to separate the multiple captured point sources and apply image processing for data detection. In this work,, for further analysis we consider the projection of one Tx on to the Rx (i.e., camera), which can also be applied to multiple captured point sources. The intensity-modulated light signal $x(t)$ is transmitted over a free space channel and is captured at the Rx using a CMOS RS-based camera. For the LOS link, the received signal is given by [24]:

$$y(t) = \eta x(t) \otimes h(t) + n(t),$$

(1)

where $h(t)$ is the combined impulse response of the channel and camera, η is the quantum efficiency of the IS, $\otimes$ is the time domain convolution and $n(t)$ is the additive white Gaussian noise including the ambient light induced shot noise and the noise in the camera (i.e., fixed pattern, thermal (FPN)), photocurrent shot (optical excess and electronics) and flicker noise sources), as shown in Fig. 1(b) [25]. Note, if the definition of power is scaled by the number of points in the signal, this gives the mean squared error (MSE). This notion can be extended in OCC for actual transmitted and received images by summing up twice the rows and columns of image vectors or stretching the entire image into a single vector of pixels and applying the one-dimensional definition. Therefore, in signal images OCC the SNR can be given as:
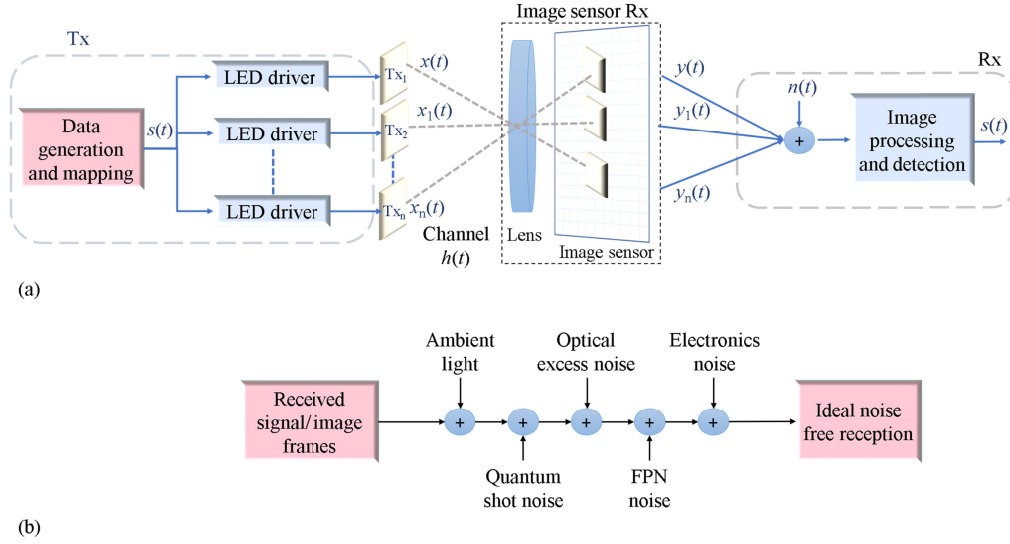
Fig. 1. (a) Schematic block diagram of MIMO-OCC link and (b) different sources of noise in OCC Rx end.

$$SNR \text{ (dB)} = 10\log_{10} \frac{\sum\limits_{m=1}^{W}\sum\limits_{n=1}^{H} I_{Tx}(m,n)^2}{\sum\limits_{m=1}^{W}\sum\limits_{n=1}^{H} [I_{Tx}(m,n) - I_{Rx}(m,n)]^2}, \tag{2}$$

where $I_{Tx}(m, n)$ and $I_{Rx}(m, n)$ denote the intensity of the pixel of the transmitted and received image frames, respectively at the location (m, n). In (2), $[I_{Tx}(m, n) - I_{Rx}(m, n)]^2$ corresponds to the squared error between original and corrupted signals as $|y(t) - x(t)|^2$. The size of the image is W (width) × H (height). High values of SNR show that, the estimation error is small and, therefore, among various image fusion methods the ones that exhibit higher SNR values can be considered for improved performance. The PSNR and the MSE are measured similar to the SNR, which are defined as [26, 27]:

$$PSNR \text{ (dB)} = 10\log_{10} \frac{I^2_{peak}}{MSE}, \tag{3}$$

$$MSE = \frac{\sum\limits_{m=1}^{W}\sum\limits_{n=1}^{H}[I_{Tx}(m,n) - I_{RX}(m,n)]^2}{N_{column} \times N_{row}}, \tag{4}$$

were I^2_{peak} denotes the squared peak intensity of the measured frame and N_{column} and N_{row} are the number of columns and rows of the images, respectively. It can be seen that, PSNR ≥ SNR. Both will be equal only when the original clean signal is constant and with the maximum amplitude. In the case of PSNR, the major focus is on the peak intensity I_{peak} of the measured frame in order to determine the signal bandwidth or number of bits to represent the signal. Therefore, the major issue is how the high-intensity regions of the image will be affected by the noise. This is much more content-specific than the SNR, which can be adopted in many applications such as image compression.

B. Developed MIMO OCC system

A simple design of the MIMO Tx unit is adopted from our previous work in [12], as illustrated in Fig. 2. It is composed of a 64-neopixel array with an 8 × 8 small chip-LED [28], see Fig. 2(a), and a 1 cm thick LED grouping grid, which is placed over the Tx LED array, see Fig. 2(b).

The LED grid is designed to divide a 64-neopixel chip-LED into 8 different column-wise groups with 8 chip-LED per group to allow 8 different data transmission channels using a single neopixel LED array. A 2 mm thick opaline methacrylate LED diffuser, commonly used, is placed over the Tx. The size of the LED array is 7.2 × 7.2 cm². The characterization of the proposed MIMO Tx unit in terms of its optical radiation pattern and output optical power-current-voltage (L_{lux}-I-V) curves was performed in [12]. Note, it is recommended to drive each LED with I_{LED} = 20 mA [12, 28]. Therefore, for the LED array the drive current $I_{LED-array}$ was set to 1.28 A for measuring L_{lux}-I-V. It was found that, the neopixels used either as a single LED chip or an LED-array together with the grid and diffuser depicted liner L_{lux}-I-V plots, which are highly desirable in IM VLC systems [12].
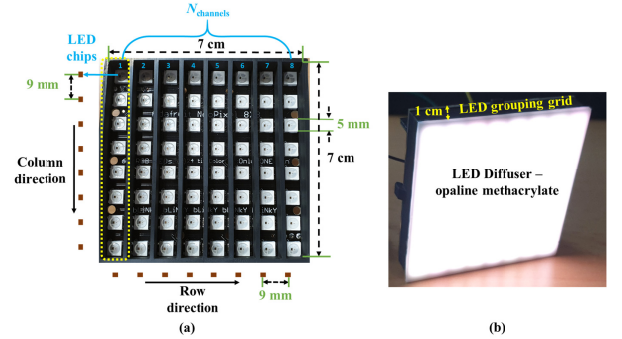

Fig. 2. Tx configuration: (a) Tx dimensions with LED grouping and (b) Tx with LED grouping grid and diffuser.

Figure 3 illustrates the data mapping on the controller side for the proposed MIMO-OCC using two 64-neopixel Tx units and Arduino Uno micro-controller-based driver per Tx. Neopixels are controlled using Arduino software. First, N_{pixels} are assigned to N_{chips} per neopixel Tx, which are then grouped column-wise into 8-$N_{channels}$. Note, in order to support rotational movements and study the angular behavior of multi-channel Txs, the rotation angle within the range of 0° < θ < 90° was changed at 10° steps, see inset (i) of Fig. 3. The data generated using Arduino unit is mapped to the LED addresses with the frequency f_s = (t_{chip})⁻¹, where t_{chip} is the 1-bit time per neopixel chip with the minimum value set to 2.5 ms due to Arduino hardware limitation to ensure flicker-free transmission at f_s of 400 Hz [12]. NRZ-OOK data bit
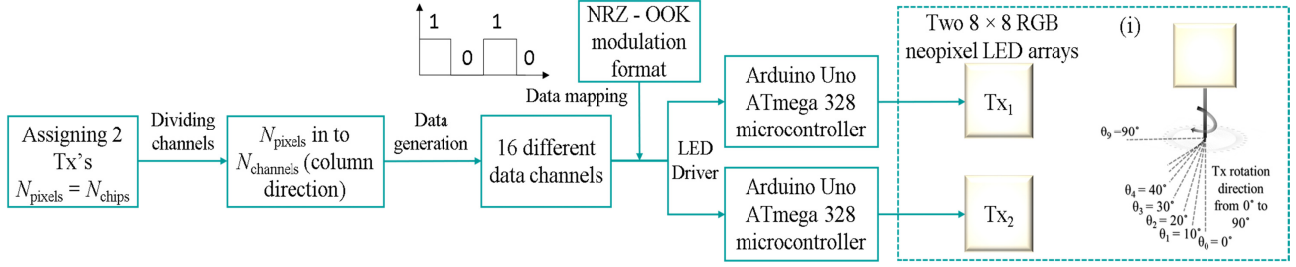
Fig. 3. Data mapping in Arduino domain: inset i) angular orientation of Tx.

streams with RGB (P_i, P_j and P_k) as $P_i + P_j + P_k = 1$ and $P_i + P_j + P_k = 0$ is used for IM of Txs for transmission over the free space channel. Note, the same data is transmitted by all 8-LEDs per $N_{channel}$ as shown in Fig. 4, while, Txs 1 and 2 are transmitting different data signals. For example, the predefined 8-bit data in $N_{channel1}$, see Fig. 4(a), is transmitted by all the 8-LEDs in the Tx_1 as shown in Fig. 2(a). Note, the data is transmitted simultaneously by all the channels in Tx_1 and Tx_2. Moreover, $N_{channel1}$ is the inverted version of $N_{channel2}$ in the Tx_1, which is adopted for synchronization of each LED group transmitting different packets. The anchor-based transmission needs considering when (*i*) transmitting long data streams via the proposed Tx design or in other techniques such as massive MIMO [6]; and (*ii*) for links experiencing blocking and shadowing [11].

Figure 5 shows an example of the RS-based capturing of the proposed multi-channel Tx. In RS-based capturing mode, the camera sequentially integrates all illuminated pixels at the exposure time $t_{rwo-exp}$, which is the same as scanning. The RS-based Rx reported in the literature capture a single bit for $t_{rwo-exp}$ [16 – 21]. Note, in RS-based cameras the readout time $t_{readout}$ ensures that there is no overlapping of rows of pixels and allows multiple exposures of a single captured image. In the proposed scheme, using multi-channel Txs 8-bit (1-bit per channel) of data are captured in a single row over $t_{rwo-exp}$, see Fig. 5, which ensures flicker-free transmission at higher R_b, in contrast to traditional RS schemes capturing only a single bit/$t_{rwo-exp}$. Note, the proposed Tx has a small surface area for capturing sufficient lights with a controller limitation defined by f_s of 400 Hz. In flicker-free transmission, R_b can be improved by increasing the surface area of the Tx unit (i.e., a higher number of LEDs).

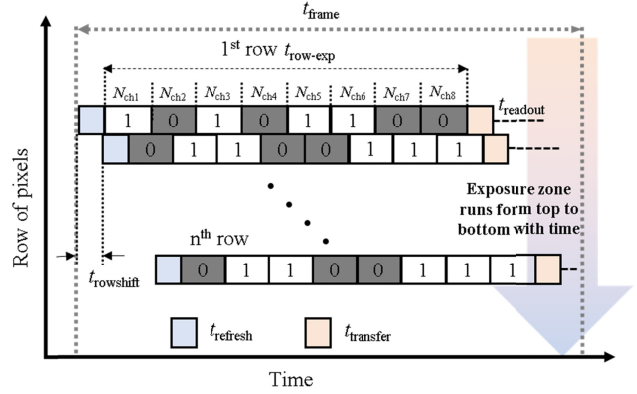Fig. 4. Transmitted bits through: (a) Tx_1 and (b) Tx_2.

Fig. 5. RS based capturing of the proposed multi-channel Tx.

The number of rows depends on R_b and the transmission distance. The maximum number of visible bits per group in a single frame and the frame time are given as:

$$N_{visible} = \lfloor t_{frame} \cdot f_s \rfloor. \tag{5}$$

$$t_{frame} \leq N_{row} \times t_{row\text{-}shift} + t_{row\text{-}exp}, \tag{6}$$

where, N_{row} is the pixel rows, which is based on the camera resolution, $t_{row\text{-}shift}$ is the row shift and t_{frame} is frame time. Note, (*i*) $t_{row\text{-}exp}$ of the last row per frame is a very small value; and (*ii*) in the RS- based capturing mode there is a delay in the start of each row, which results in $t_{row\text{-}shift}$. It was shown in [12] that, $N_{visible}$ will change with respect to the distance between the Tx and the Rx as well as camera resolution. Based on $N_{visible}$, the data transmission rate is given as:

$$R_b = N_{channels} \times f_s, \tag{7}$$

where $N_{channels}$ is the number of LED groups in the Tx unit.

C. Detection scheme to study the Tx angular rotation influence

Figure 6 illustrates the flowchart for the detection when considering the Tx's angular rotation as $0° < \theta < 90°$ in the proposed systems. At the Rx, we have used a RaspiCam with given SS, resolution and frame rate for capturing images (i.e., recording a video stream for 5 s) of IM light sources over L of 30 to 110 cm. The overall detection process is divided into 3 main stages, as follows:

Stage 1: Video recording and frame division: The RaspiCam Rx records data and calibration video streams that represent the captured transmitted information and the Tx's template shape, respectively. The calibration videos, which outline the intensity compensation of the data video frames, are used for equalization. As IS captures multiple light Txs as different point sources on different sections of the IS. Therefore, the image frame is divided to distinguish multiple light sources for detection. Note, a
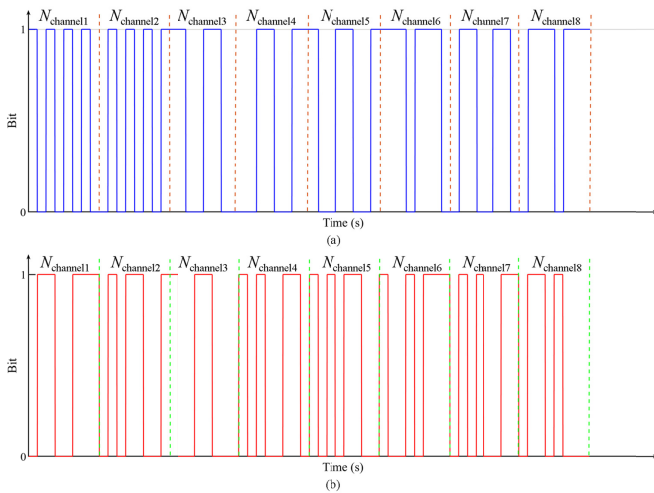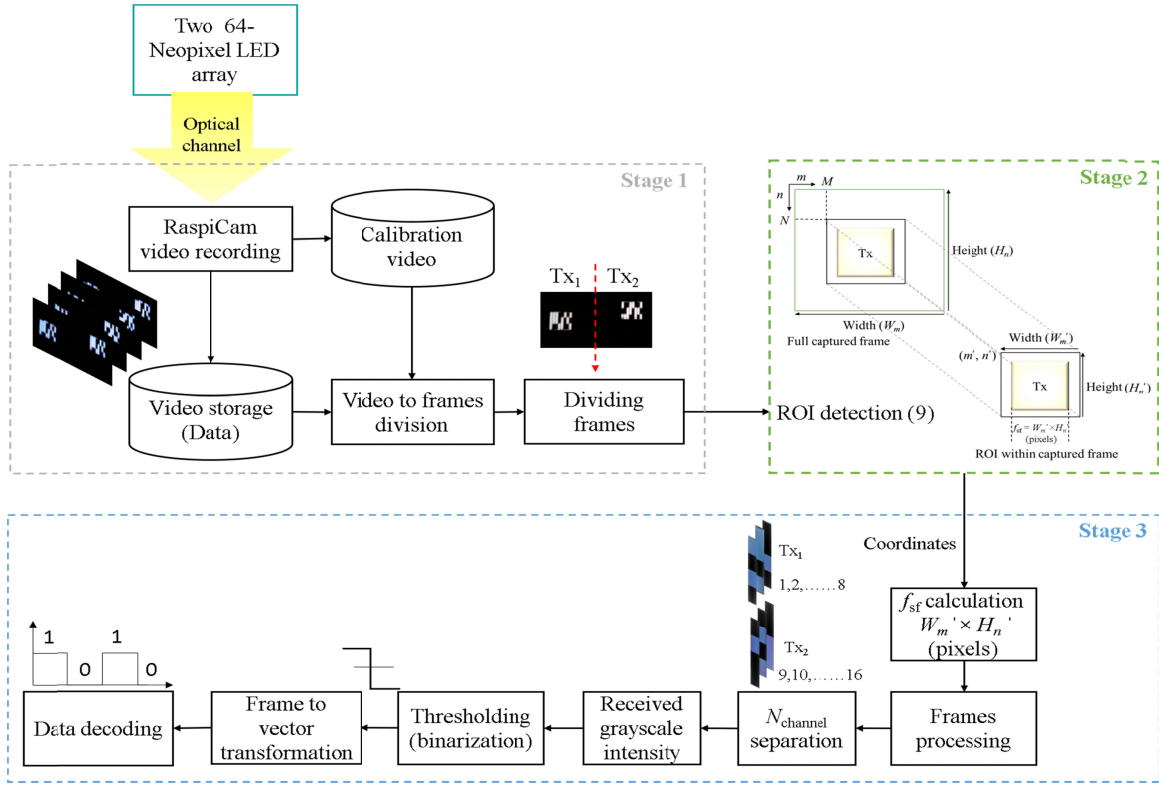
Fig. 6. Flowchart illustrating the data detection process.

considerable smaller image containing the signal information is transmitted in order to reduce the processing time at the Rx.

Stage 2: Region of interest (ROI) detection: Here, we perform ROI detection [29] over the divided frames, and then use the obtained coordinates, which define boundaries of the ROI, for image cropping. The ROI template used to define ROI in the full calibration capture frame. It is given as:

$$ROI = (m', n', W_m', H_n'), \tag{8}$$

where m' and n' are top corner coordinates, and W'_m and H'_n are the width and height of the captured image frame, respectively. Here, we have adopted an image processing technique known as template matching [30] to determine the target ROI in the calibration image frame and then to find the position of the target ROI_{temp} in the data image frame, given as [30]:

$$ROI_{temp} = \sum_{m=0}^{W_m} \sum_{n=0}^{H_n} \{P(m', n') - P'(M + m', N + n')\}^2, \tag{9}$$

where the coordinate of a single point in ROI is (m', n') with a pixel value $P(m', n')$, while the coordinate of the overlapping point and its pixel value are $(M + m', N + n')$ and $P'(M + m', N + n')$, respectively. The overlapping points of the data image frame and ROI image are calculated using template matching. The coordinate (M, N) is the origin of the template image on the full captured image. It is assumed that, the sizes of the template and the fully captured input image are $W_m' \times H_n'$ (width × height) and $W_m \times H_n$ (width × height), respectively. ROI_{temp} obtained from (9) is used to crop the data image frames. The values of ROI_{temp} need to change dynamically as in this technique the shape of the Tx unit changes with θ and the distance between the Tx and the camera settings. This technique can be further adapted to detect multiple ROI's within a single image frame based on its template coordinate points.

Stage 3: Frame processing and data detection: The ROI cropped images from the previous stage are used to calculate the spatial frequency components f_{sf}, which refers to the projection of a target, i.e., the Tx LED array over a captured image in terms of pixels [30]. As shown in Stage 3 of Fig. 6, in terms of pixels f_{sf} of ROI_{temp} is $W_m' \times H_n'$. Next, f_{sf} separated images are processed for $N_{channel}$ separation followed by image processing. As outlined in Stage 3 of Fig. 6, each $N_{channel}$ is converted from the RGB color format to the grayscale for both calibration and data frames in order to retrieve the intensity profile. As the intensity levels for NRZ-OOK data signals are set as $P_i + P_j + P_k = 1$ (with $I_{peak} = 255$) and $P_i + P_j + P_k = 0$, the threshold level is set based on the average of the received image intensity profile in ROI. Following thresholding, binarization of the data frames is performed to convert the frame into vector transformation, which is applied to the remaining frames for decoding the transmitted data bit streams. Finally, the received data bit vector is then compared with the transmitted data to ascertain the success of reception of received bits by determining the ratio of the wrongly decoded bits to the total number of transmitted bits (i.e., the number of bit error).

3. MEASUREMENT SETUP

The measurements were performed for two different transmission setups as illustrated in Fig. 7. As previously mentioned, we focus on the investigation of angular rotation of Tx units within multichannel OCC. Both Tx units rotate with θ of 0° to 90°. A Raspberry Pi camera used as a Rx is mounted at the top of display panel at a height h_{Rx} of 18 cm and an angle θ_c of 90°, see Fig. 7. In both the setups, the radial distance r between the Tx₁ and Tx₂ is changed with respect to the transmission length L between camera and the Txs. Note, r was increased to ensure that both Tx units are captured at the same time in a single image frame.

i) *Transmission setup1*: Both Tx units are placed at the same distance but different heights h_{Tx_1} (same as the camera height h_{Rx}) and h_{Tx_2} at 25 cm, see Fig. 7(a). Note, the actual transmission distance between both Tx units and camera is $l = \sqrt{L^2 + (\frac{r}{2})^2}$, see Fig. 7(a). For example, for L and r of 30 and 20 cm l is ~ 32 cm. Note, the difference between L and l is rather small therefore, for further analysis and simplicity we will only use L.

ii) *Transmission setup 2:* Both Tx units are placed at the same height $h_{Tx} = h_{Rx}$ but at different distances, L_1 and L from the camera, see Fig. 7(b), where $(L_1 - L) = 30$ cm.

The experimental setups for investigating the angular behavior of the proposed MIMO-OCC scheme are shown in Fig. 8.
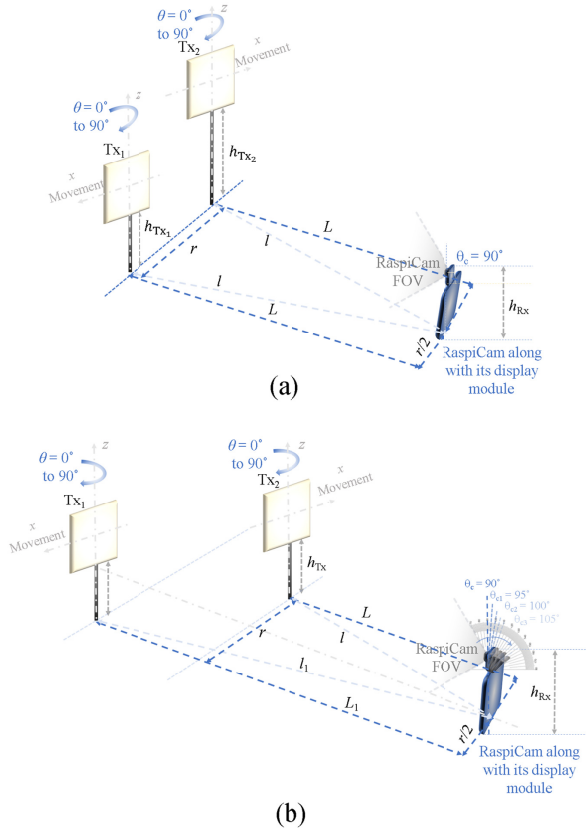

(a)

(b)

Fig. 7. Transmission setups: (a) Tx units placed at different heights and (b) Tx units placed at a different distance.
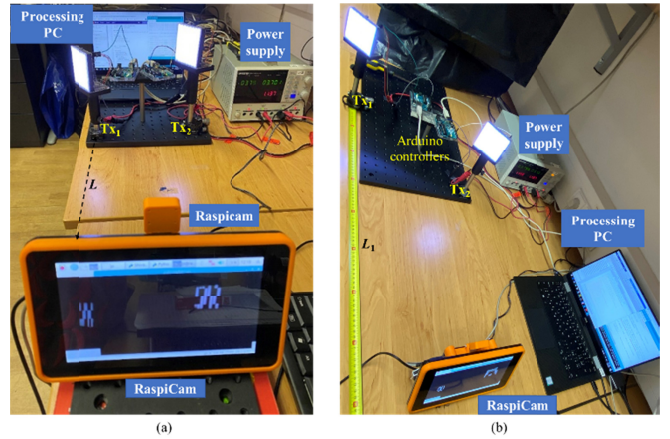

(a)   (b)

Fig. 8. Experiment setup: (a) Tx units placed at different heights and (b) Tx units placed at a different distance.

The Tx units are controlled using an Arduino Uno board, which is an open-source microcontroller board based on ATmega328 [32]. A 64-bit long data stream (i.e., 8-bit per group, see Fig. 4) is generated in Arduino software domain for each Tx unit and mapped to each LED (i.e., address) using Arduino Uno board. The key experimental parameters are listed in Table 1. The camera used is Raspberry Pi (PiCamera V2), which is based on Sony IMX219 sensor [33]. RaspiCam is attached to Raspberry touchscreen display to provide easy interface and control over the camera capturing modes and settings. Experiments were performed for nine transmission distances and three different values of SS (see Table 1) for θ of 0° to 90°. The NRZ-OOK signal was recorded for 5 second (a total of 150 frames).

Table 1. Key parameters of the experiment setup.

Parameter	Value
RaspiCam chip size	5.09 mm (H) × 4.930 mm (W) Diagonal: 4.60 mm
RaspiCam resolution	1920 × 1080 pixels
Raspberry display size	7" (diagonally)
Raspberry display resolution	800 × 400 pixels
t_{chip}	2.5 ms
f_s	400 Hz
RaspiCam frame rate	30 fps
N_{row}	1080 pixels
Tx	8 × 8 RGB neopixel LED array
$N_{channels}$	16 LED groups with 8 groups each Tx and 8LED/group
$I_{LED-array}$	1.28 A (for each Tx unit)
t_{frame}	0.216 ms
SS	200, 400 and 800 μs
R_b	6.4 kbps
L	30 – 110 cm
L_1	60 – 140 cm
r	25 – 45 cm
Tx Rotation angle θ	0° – 90°
Rx angle θ_c	90°

4. EXPERIMENT RESULTS AND ANALYSIS

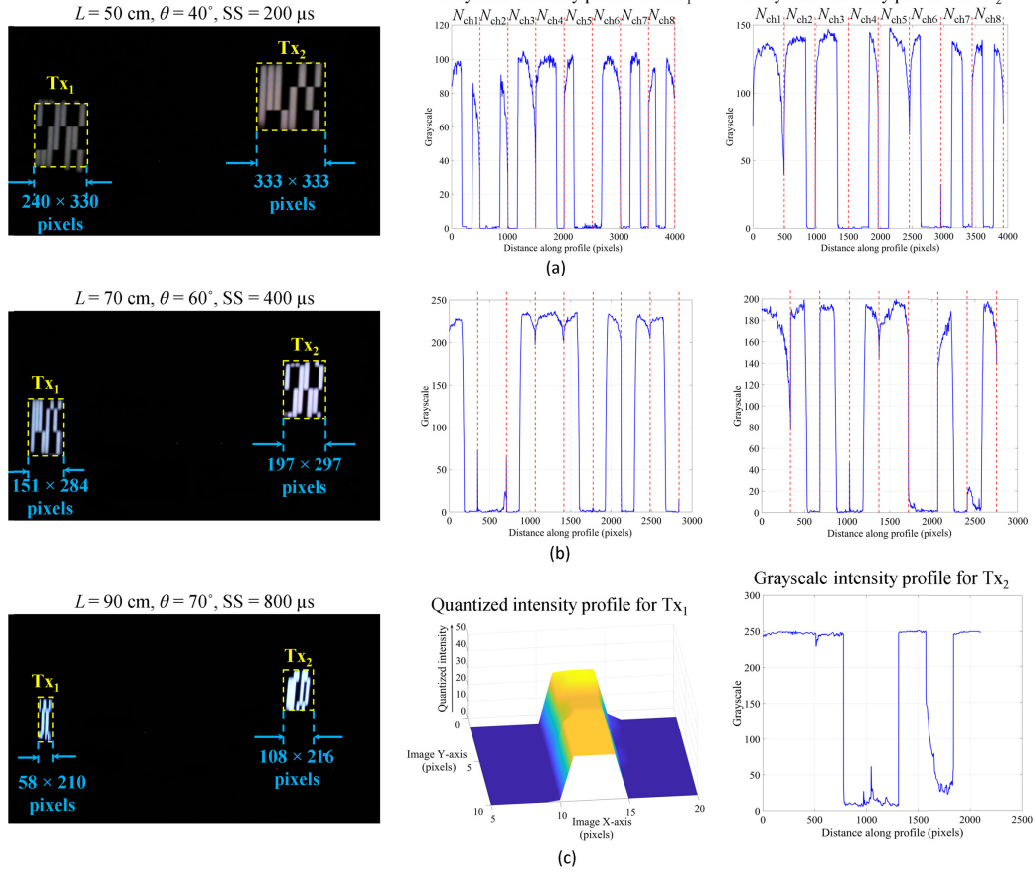### A. Tx units placed at the same distance and different heights

Fig. 9. The grayscale and quantized intensity profiles of originally captured images for data detection at: (a) L of 50 cm, θ of 40° and SS of 200 μs, (b) L of 70 cm, θ of 60° and SS of 400 μs and (c) L of 90 cm, θ of 70° and SS of 800 μs.

Figure 9(a)-(c) show examples of captured image frames, f_{sf}, and the grayscale intensity profiles for the detected data per $N_{channels}$ for a range of L, θ and SS. It can be seen that, the shape of the captured Tx changes due to angular tilting, which results in the loss of data bits. To avoid this, the first and last pixel rows in each image frame are eliminated from the top and bottom of each Tx ROI. The received intensity distribution within the image frame is shown in the form of grayscale intensity profiles for the captured original images. These intensity profiles play an important role in determining the higher and lower intensities (i.e., representing 1 and 0) in the received image frames for further thresholding and demodulation [11]. The dotted yellow box in the original image frames defines the ROI, which fills only f_{sf} of the captured Tx within the full image frame. The clear and sharp distinction between the data lines can be seen for θ up to 40°, L and SS of 50 cm and 200 μs, respectively, see Fig. 9(a). While the lines get saturated for higher values of θ, which reduces f_{sf} and SS, see Figs. 9(b) and (c), thus making it challenging to separate $N_{channels}$ and therefore, affecting data demodulation (i.e., higher number of error bits). We have therefore shown the intensity distribution in the form of quantized intensity profile of the captured image frame for θ of 70°, L of 90 cm and SS of 800 μs, see Fig. 9(c). Therefore, data detection at L up to 110 cm was performed for θ up to 80° with SS of 200 and 400 μs, and θ of 70° with SS of 800 μs.

Table 2 shows the average f_{sf} of the captured Tx image with respect to L and θ. It can be seen that, f_{sf} (reduces) and the shape (square to rectangle) of Tx 's changes with L and θ. Note, considering the average f_{sf} we see very little changes in L (10 cm) and θ (10°). For L of 30-50 cm, f_{sf} has ~2 and 3 times more high-frequency components than for L

of 60-90 cm for a range of θ, see Fig. 9(a)-(c). Therefore, it can be said that a reduced number of pixels of the Tx image leads to lower high-frequency components, and consequently, the channel can be seen as a low-pass filter with a cut-off frequency that decreases with increasing L and θ. Further analysis is performed for f_{sf} at different values of L and θ and its impact on communications link performance in terms of the successful reception and PSNR.

Table 2. Average f_{sf} in pixels with respect to L and θ (upper values are for the Tx$_1$ and bottom for the Tx$_2$).

L (cm)	θ 0° – 20°	θ 30° – 50°	θ 60° – 80°
30 – 50	450×450	210×310	200×300
	459×459	300×300	171×290
60 – 80	155×285	150×280	145×260
	200×299	195×294	185×285
90 – 110	78×230	65×215	55×200
	115×240	105×235	100×215

Figure 10 (a) then illustrates the performance analysis of the angular behavior of multi-channel MIMO-OCC link in terms of the percentage success of the received bits with respect to θ for various values of L and SS. In this setup, the average time window for offline OCC data extraction (only) was about 0.98 s using a predefined data processing algorithm depicted in Fig. 6. It can be seen that, for L up to 80 cm, 100 % reception success is achieved for θ of 50° for SS of 200 and 400 μs; and for θ of 30° for SS values of 800 μs, see Fig. 10(a). Note,
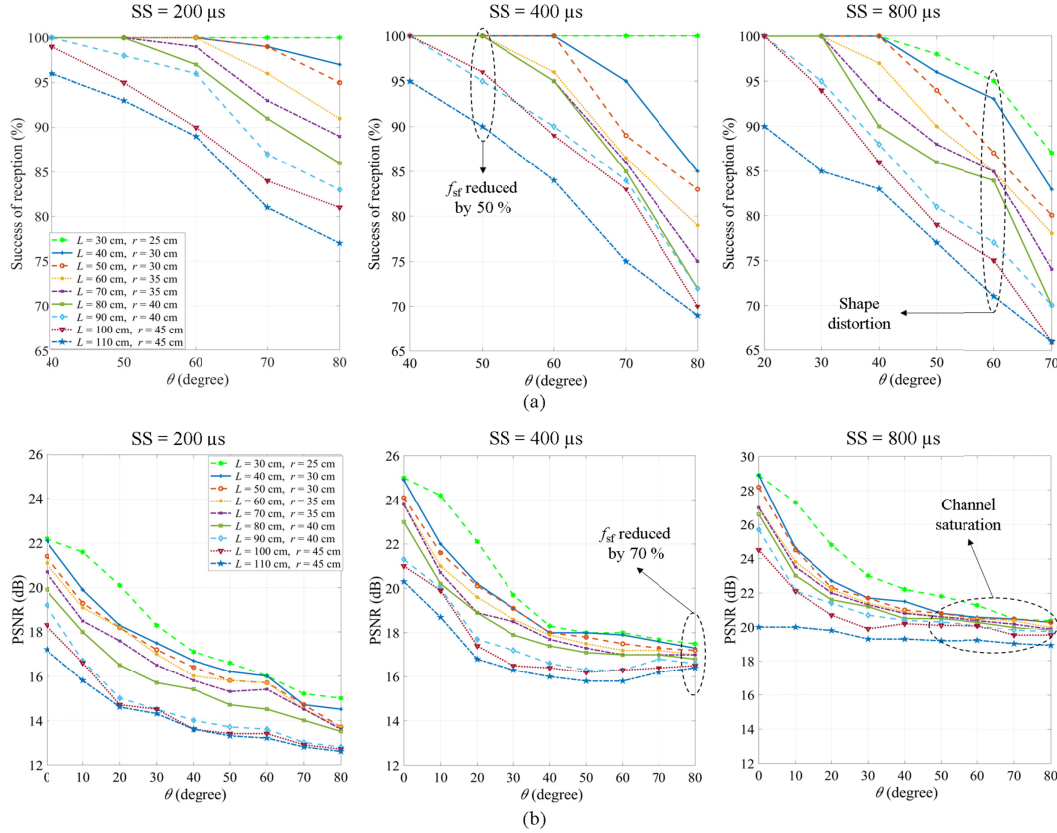
Fig. 10. Performance analysis: (a) success of reception and (b) PSNR

for L of 30 cm, 100 % success is achieved for θ of 0° to 80° and for SS values of 200 and 400 μs. It can also be seen that, the reception success reduces further with f_{sf} (i.e., less than ~50 % at θ of 0°, see Table 2), and increase with SS, which results in channel saturation. Thus, making it challenging to separate $N_{channels}$ and therefore, the decoding of received bits, see Figs. 10(a).

As previously mentioned in Section 2, in OCC, the data is captured in the form of a two-dimensional image, therefore the conventional SNR measurement cannot fully reflect the quality of the link. Here, we have adopted PSNR, which is widely used as a quality metric in image processing systems. Equations (3) and (4) are used to compute the MSE between the transmitted and received images with respect to ROI$_{temp}$ (Eq. (9)) as given by:

$$\text{MSE} = \frac{\sum_{m=1}^{W_m}\sum_{n=1}^{H_n}[\text{ROI}_{temp}(m,n) - I_{RX}(m,n)]^2}{W_m \times H_n}. \quad (10)$$

As the input image has an 8-bit unsigned integer data type with $I_{peak}^2 = 255$, the PSNR is computed by substituting (10) and I_{peak}^2 in (3). Figure 10(b) shows the performance of the OCC link in terms of PSNR with respect to θ for different values of SS and link spans. As shown, PSNR increases with SS due to the fact that, the images of captured Tx at higher SS are more saturated compared with those captured at lower SS, see Fig. 9(c). Note, the PSNR decreases with decreasing f_{sf} (70 % than at θ of 0°, see Table 2 and Fig. 10(b)) with respect to θ and L. This is due to the fact that, the Tx units move away from the camera field of view with increasing θ and L therefore, a small amount of light passes through the camera lens and hence fewer photons are incident on the pixels of the image sensor and thus reduced f_{sf}. With 100 % reception success, the PSNR value of ~22 dB is measured for SS of 200

μs, which is increasing by 3 and 7 dB for SS of 400 and 800 μs, respectively for L of 30 cm at θ of 0°.

Based on $N_{channel}$ and $N_{visible}$ for each Tx unit in the image frames, the data throughput is given as:

$$\text{Data throughput} = N_{channel} \times N_{visible} \times (\frac{\text{fps}}{2}). \quad (11)$$

Figure 11 illustrates the performance analysis of the proposed multi-channel MIMO-OCC in terms of data throughput calculated with respect to θ and L. For θ of 0° the maximum data throughput of 1.92 kbps is observed for L of 30 cm, where 8-bit data stream (4-bit/$N_{channel}$/Tx) is seen by the camera. f_{sf} is decreased with increasing L and θ, thus resulting in reduced $N_{visible}$ and data throughput. For θ of 40° the data throughput of 1.44 kbps is observed for L of 50 cm, where a 6-bit data stream (3-bit/$N_{channel}$/Tx) is seen by the camera, see Fig. 9(a). For L of 90 to 110 cm, 2-bit stream (1-bit/$N_{channel}$/Tx) are visible to the camera, see Fig. 9(c) and therefore the data throughput of 480 bps is obtained for each θ.
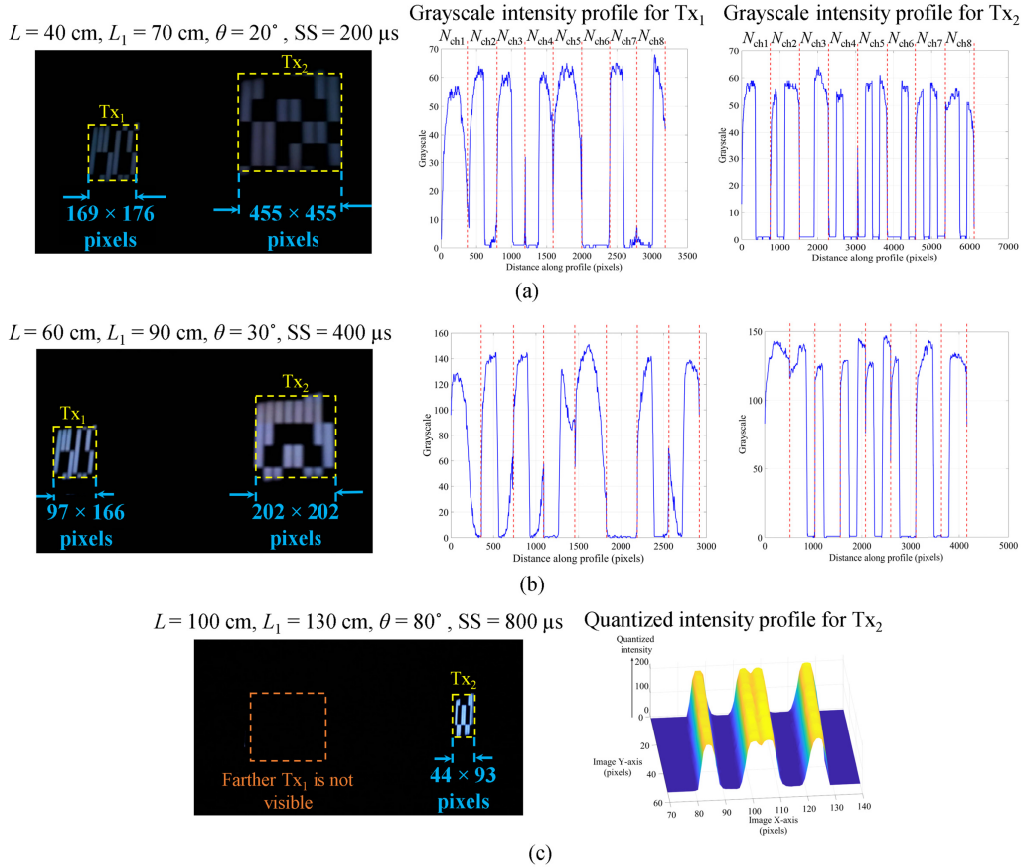
Fig. 12. The grayscale and quantized intensity profiles of originally captured images for data detection at: (a) L of 40 cm, θ of 20° and SS of 200 μs, (b) L of 60 cm, θ of 30° and SS of 400 μs and (c) L of 100 cm, θ of 80° and SS of 800 μs.
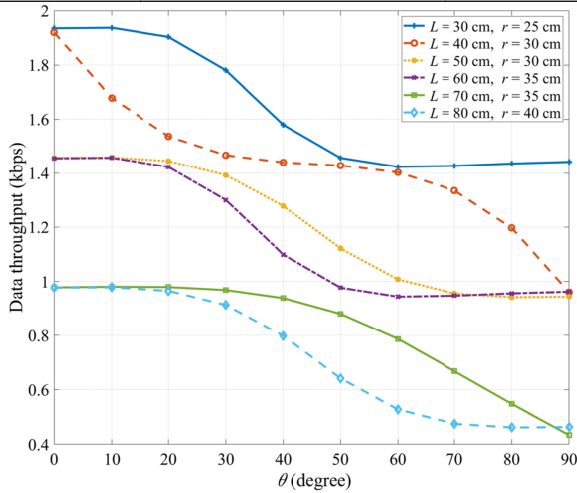

Fig. 11. Data throughput with respect to change in L and θ.

B. Tx units placed at different distances

Figure 12 shows the captured image frames, f_{sf} and the grayscale intensity profiles of the detected data for each $N_{channels}$, L, θ and SS. The clear and sharp distinction between the data lines can be seen at θ of 20° and 30°, L of 40 and 60 cm and SS of 200 and 400 μs, respectively, see Fig. 12(a). Note, in this setup, due to increasing tilting angle θ, the

Tx_1 at L_1 of 130 cm is not visible and the Tx_2 at L of 100 cm is too small to separate $N_{channel}$ for demodulation, see Fig. 12(c). Therefore, data detection was carried out for L up to 90 cm at θ up to 70° for all values of SS.

Table 3 shows the average f_{sf} of the captured Tx image with respect to L and θ. f_{sf} for the Tx_2 (closer to the Rx) at L of 30-40 cm has ~2 to 3 times more high-frequency components than the Tx_1 (closer to the Rx) for L of 60-70 cm with respect to θ, see Fig. 9(a)-(c). In this case, it can be said that the large reduction in f_{sf} of the Tx image is due to r between the Txs. An increase in r and θ reduces f_{sf}, which results in higher bit errors and lower PSNR.

Table 3. Average f_{sf} in pixels with respect to ranges of L and θ. (upper values are for the Tx_1 and bottom for the Tx_2).

L and L_1 (cm)	θ 0° – 20°	θ 30° – 50°	θ 60° – 70°
60 – 70	165×175	160×210	148×200
30 – 40	450×451	349×351	170×289
80 – 90	210×210	190×200	125×155
50 – 60	100×170	95×165	80×150
90	100×160	70×150	56×175
120	80×155	50×140	40×100

Figures 13(a) and (b) illustrate the performance analysis of the angular behavior of multi-channel MIMO-OCC link in terms of percentage of success of the received bits and PSNR. In this setup, the average time window for offline OCC data extraction (only) was about
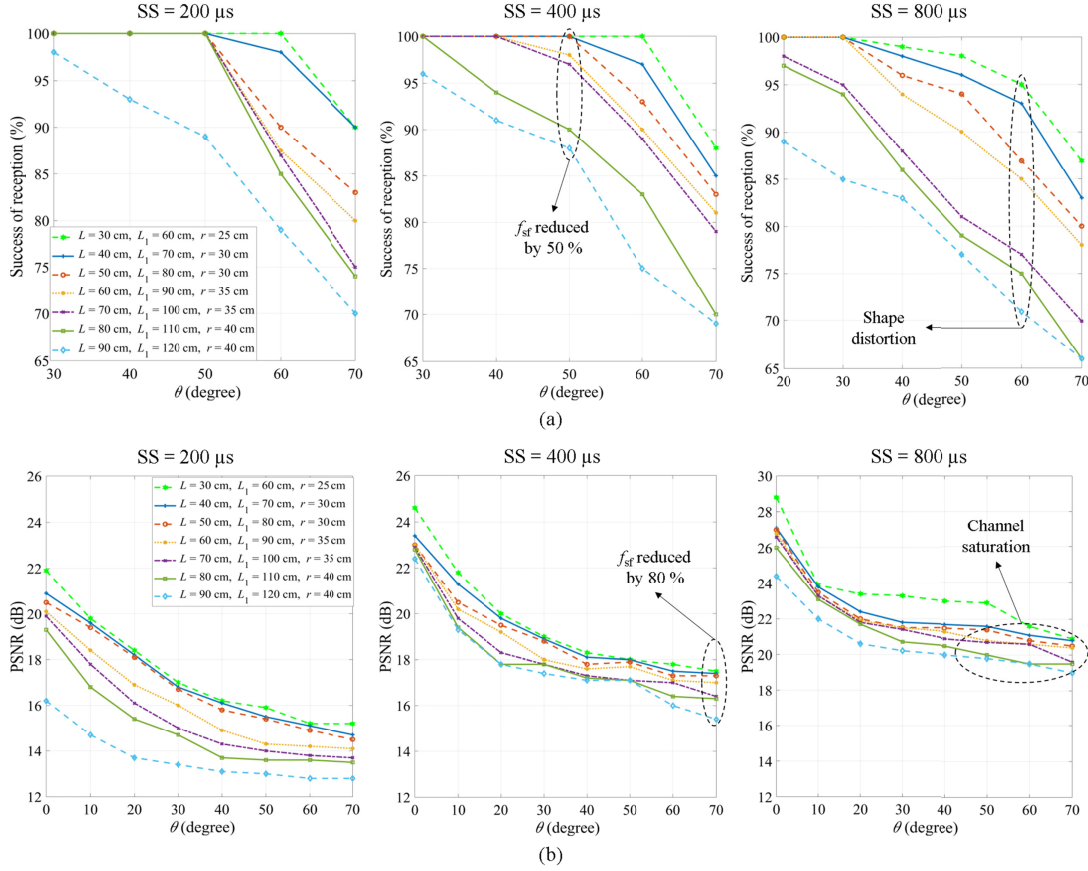
Fig. 13. Performance analysis: (a) success of reception and (b) PSNR.

1 s using a predefined data processing algorithm, see Fig. 6. It can be seen that, for L and L_1 of up to 60 and 90 cm, 100 % success is achieved for θ of 40˚ with SS of 200 and 400 μs and for θ of 30˚ with SS of 800 μs, see Fig. 13(a). As previously mentioned, the data reception success is also affected by f_{sf}. Note, in this setup the Tx_1 is placed farther than the Tx_2 with respect to the camera. Therefore, with the increasing L and θ, f_{sf} becomes smaller (f_{sf} is reduced by 80 % for θ increasing from 0˚ to 70˚ for all values of L, see Table 3 and Fig. 13(b)). Note at $L = 100$ cm and $L_1 = 130$ cm the Tx_1 is no longer seen by the camera, see Fig. 12(c). The PSNR of ~13 dB is measured for SS of 200 μs, which is increased by 2 and 6 dB for SS of 400 and 800 μs, see Fig. 13(b), respectively for L of 90 cm at θ of 70˚. The maximum PSNR of 22, 25 and 29 dB are observed for SS of 200, 400 and 800 μs, respectively for L of 30 cm and θ of 0˚.

Figure 14 illustrates the data throughput as a function of θ for the proposed multi-channel MIMO-OCC system. The data throughput decreases with f_{sf} due to the increased link span and θ. For θ of 0˚, the maximum data throughput of 1.68 kbps is observed at L of 40 cm, where the 7-bit data stream (3-bit/$N_{channel}$ for Tx_1 and 4-bit for Tx_2, is visible to the camera. For θ of 30˚, the data throughput is reduced by 480 bps for L of 60 cm, and only 5-bit (2-bit/$N_{channel}$ for Tx_1 and 3-bit for Tx_2, see Fig. 12(b), are captured by the camera.

We have shown results for both setups in terms of the success rates of received bits, PSNR and data throughput. E.g., a 100 % success rate with PSNR of ~ 14 and 17 dB were achieved for θ of 50˚, L of up to 80 cm and SS of 200 and 400 μs, respectively. Note, in this case f_{sf} was reduced by up to ~50 % compared with f_{sf} obtained in case of Txs without the inclusion of rotation. The maximum data throughputs of 1.9 and 0.9 kbps were achieved at θ of 0˚ and 50˚, respectively for L of

up to 60 cm. Note, a higher data throughput of 1.9 kbps is observed for the transmission setup 1 due to the Tx units being located in the same plane, whereas in the transmission setup 2 the data throughput is reduced to 1.68 kbps as the Tx units are placed apart from each other at ($L_1 - L$), see Fig. 7(b). Therefore, the difference in the distances between Tx units results in decreased f_{sf}, which leads to lower $N_{visible}$ and reduced data throughput.
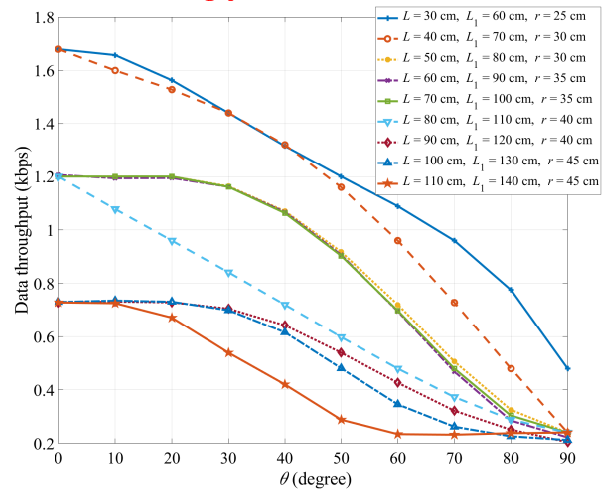

Fig. 14. Data throughput with respect to change in L and θ.

5. CONCLUSIONS

In this paper, we demonstrated f_{sf} based angular behavior of multi-channel MIMO-OCC for two different transmission setups where the Tx units are placed at different heights and distances from each other and the camera. We showed that, the proposed study provided a 100 % success rate in data reception at the optimum θ up to 50° for both the transmission setups at lower captured values of f_{sf}, which is projected onto the image sensor in the form of pixels. We provided a general solution based on f_{sf} to investigate the MIMO-OCC considering the angular movement of the Txs. The proposed study can be adopted for longer transmission distances based on f_{sf} and employing a Tx with a larger illuminating surface area for use in indoor environments. E.g., using Txs with surface areas of 14×14 cm², L can be extended to 1.6 m (i.e., 2×L) and placing the Tx units at r of 80 cm apart can provide an optimum angle $\theta > 50°$ for each case.

Unlike LOS and NLOS OCC links, the proposed system can be further adopted in indoor IoT-based links with multi-Txs/Rxs and mobility, offer an improved solution when consideration of the optimum angular orientation of multiple Tx units is critical. Although the small-scale experiments were only conducted for demonstration purposes, it is envisioned that the proposed study can readily be expanded using image processing techniques such as shape restoration using neural networks and code extraction techniques to improve the success rate of received bits.

Disclosures. The authors declare no conflicts of interest.

References

1. M. J. Jang, "IEEE 802.15 WPAN 15.7 amendment-optical camera communications study group (SG 7a)," [Online accessed 18 May 2020] 2020.
2. R. Boubezari, H. Le Minh, Z. Ghassemlooy and A. Bouridane, "Smartphone Camera Based Visible Light Communication," in Journal of Lightwave Technology, **34** (17), 4121-4127, 1 Sept.1, 2016,
3. Z. Ghassemlooy, L. N. Alves, S. Zvanovec, and M.-A. Khalighi, Visible Light Communications: Theory and Applications (CRC Press, 2017).
4. IEEE Standard for Local and Metropolitan Area Networks—Part 15.7: Short-range wireless optical communication using visible light, IEEE Standard 802.15.7-2011, 1–309, Sep. 2011.
5. C. Jurado-Verdu, V. Matus, J. Rabadan, V. Guerra, and R. Perez-Jimenez, "Correlation-based receiver for optical camera communications," Opt. Express **27**, 19150-19155, 2019.
6. W. Huang, P. Tian and Z. Xu, "Design and implementation of a real-time CIM-MIMO optical camera communication system," Opt. Express, **24**, 24567-24579, 2016.
7. M. Uysal, et al., "Optical camera communications. In Optical wireless communications," Springer, Switzerland, 547-568, 2016.
8. IEEE 802.15. Documents TG7r1. [(accessed on 24 April 2020)]. Available online: https://mentor.ieee.org/802.15/documents?n=2&is_dcn=DCN%C%20Title%2C%20Author%20or%20Affiliation&is_group=007a.
9. Panasonic news release. Start the business of information collaboration services using the 'Hikari ID' technology. Available online: http://news.panasonic.com/press/news/data/2015/12/jn151209-3/jn151209-3.html .
10. M. Shahjalal, M. K. Hasan, M. Z. Chowdhury, and Y. M. Jang, "Smartphone Camera-Based Optical Wireless Communication System: Requirements and Implementation Challenges," Electronics, **8**, 2019.
11. S. R. Teli, S. Zvanovec and Z. Ghassemlooy, "Performance evaluation of neural network assisted motion detection schemes implemented within indoor optical camera based communications," Opt. Express, **27**, 24082-24092, 2019.
12. S.R. Teli, V. Matus, S. Zvanovec, R. Perez-Jimenez, S. Vitek, Z. Ghassemlooy, "Optical Camera Communications for IoT–Rolling-Shutter Based MIMO Scheme with Grouped LED Array Transmitter," Sensors, 20, 3361, 2020.
13. C.-W. Chow, C.-Y. Chen, S.-H. Chen, "Visible light communication using mobile-phone camera with data rate higher than frame rate," Opt. Express, **23**, 26 080–26 085, 2015.
14. V. P. Rachim and W. Chung, "Multilevel intensity-modulation for rolling shutter-based optical camera communication," IEEE Photonics Technology Letters, **30** (10), 903-906, 15 May, 2018.
15. W. Wang, C. Chow, C. Chen, H. Hsieh and Y. Chen, "Beacon jointed packet reconstruction scheme for mobile-phone based visible light communications using rolling shutter," IEEE Photonics Journal, **9** (6), 1-6, Dec. 2017.
16. V. Nguyen et al., "High-rate flicker-free screen-camera communication with spatially adaptive embedding," IEEE INFOCOM 2016 - The 35th Annual IEEE International Conference on Computer Communications, San Francisco, CA, 2016, 1-9.
17. K. L. Hsu, et al., "CMOS camera based visible light communication (VLC) using grayscale value distribution and machine learning algorithm," Optics Express, **28,** 2427-2432, 2020.
18. Y. Yang, J. Hao and J. Luo, "CeilingTalk: lightweight indoor broadcast through LED-camera communication," IEEE Transactions on Mobile Computing, **16** (12), 3308-3319, 1 Dec. 2017.
19. N. Bani Hassan, et al. "Non-line-of-sight MIMO space-time division multiplexing visible light optical camera communications" Journal of Lightwave Technology, **37**, 2409-2417, 2019.
20. N. Bani Hassan, Z. Ghassemlooy, S. Zvanovec, P. Luo, and H. Le-Minh, "Non-line-of-sight 2×N indoor optical camera communications," Appl. Opt. **57**, B144-B149, 2018.
21. W.-C. Wang, C.-W. Chow, L.-Y. Wei, Y. Liu and C.-H. Yeh, "Long distance non-line-of-sight (NLOS) visible light signal detection based on rolling-shutter-patterning of mobile-phone camera. Opt. Express, **25**, 10 103–10 108, 2017.
22. W. A. Cahyadi and Y. H. Chung, "Wide receiver orientation using diffuse reflection in camera-based indoor visible light communication," Optics Communications, **431**, 19-28, 2019.
23. C.-W. Chow, et al., "Decoding CMOS Rolling-Shutter Pattern in Translational or Rotational Motions for VLC," IEEE Photonics Journal, **11** (2), 1-5, 2019.
24. Q. N. Pham, V.P. Rachim, J. An and W.-Y. Chung, "Ambient Light Rejection Using a Novel Average Voltage Tracking in Visible Light Communication System," Appl. Sci. **7**, 670, 2017.
25. F. de Souza Campos, J. A. C. Ulson, J. W. Swart, M. J. Deen, O. Marinov and D. Karam, "Temporal noise analysis and measurements of CMOS active pixel sensor operating in time domain," 2013 26th Symposium on Integrated Circuits and Systems Design (SBCCI), Curitiba, 2013, 1-5.
26. Q. Wang, Y. Shen and J. Jin, "Performance evaluation of image fusion techniques," Image Fusion, Academic press, pp. 469-492, 2008
27. J. Price and T. Goble, "Signals and noise," in Telecommunications Engineer's Reference Book, Butterworth-Heinemann, 1993, 10-1-10-15.
28. Philip Burgess. Adafruit neopixel uberguide. WS2812B Datasheet, April 2019.
29. M. D. Thieu, T. L. Pham, T. Nguyen and Y. M. Jang, "Optical-RoI-signaling for vehicular communications," IEEE Access, **7**, 69873-69891, 2019.
30. C. Xiu, R. Wang, Hybrid tracking based on camshift and template matching, in: 29th Chinese Control and Decision Conference (CCDC), Chongqing, (2017), 5753-5756.
31. S. Arnon, "Visible Light Communication Cambridge," U.K.:Cambridge Univ. Press Feb. 2015.
32. Atmel Corporation, "8-bit Microcontroller with 4/8/16/32K bytes in-system programmable flash," Atmel datasheet, 2009.

33. IMX219PQH5-C Datasheet. Available online: https://datasheetspdf.com/pdf/1404029/Sony/IMX219PQH5-C/1 (accessed on 28 January 2020).